Journal of Molecular Structure 1234 (2021) 130190

Contents lists available at ScienceDirect

Journal of Molecular Structure

journal homepage: www.elsevier.com/locate/molstr

Syntheses, crystal structures, antioxidant, in silico DNA and SARS-CoV-2 interaction studies of triorganotin(IV) carboxylates

Tariq Ali[a,b], Niaz Muhammad[a,*], Zafar Ali[a], Abdus Samad[c], Mohammad Ibrahim[a], Muhammad Ikram[a], Sadia Rehman[a], Shaukat Shujah[d], Gul Shahzada Khan[e], Abdul Wadood[c], Saqib Ali[f], Carola Schulzke[g]

[a] Department of Chemistry, Abdul Wali Khan University, Mardan Pakistan
[b] Soochow Institute for Energy and Materials Innovations, College of Energy, Soochow University, Suzhou 215006, China
[c] Department of Bio-Chemistry, Abdul Wali Khan University, Mardan, Pakistan
[d] Department of Chemistry, Kohat University of Science & Technology, Kohat, Pakistan
[e] Department of Chemistry, College of Science, University of Bahrain, Sakhir 32038, Bahrain
[f] Department of Chemistry, Quaid-I-Azam University Islamabad, 45320, Pakistan
[g] Institut für Biochemie, Universität Greifswald, Felix-Hausdorff-Straße 4, 17489, Greifswald, Germany

ARTICLE INFO

Article history:
Received 9 November 2020
Revised 11 February 2021
Accepted 22 February 2021
Available online 25 February 2021

Keywords:
Organotin(IV) carboxylates
Crystal structure
DFT
Antioxidant
Molecular docking
SARS-CoV-2

ABSTRACT

Triorganotin(IV) carboxylate complexes R_3SnL, where $R = C_4H_9$ (**1**), CH_3 (**2**) and L = 2-chlorophenyl ethanoate, were synthesized and characterized by elemental analysis, FT-IR, NMR (^1H, ^{13}C, ^{119}Sn) and X-ray single crystal analysis. The solid state analyses confirmed a bridging bidentate coordination mode for the carboxylate ligand rendering the tin ion a penta-coordinated center in the synthesized complexes. NMR spectra revealed a change in the coordination number (5→4) for tin when in the solution. The structural geometry and the electronic properties of complexes were calculated by using the density functional theory (DFT) method at B3LYP level 6–31G(d, p) and Lanl2DZ basis sets. A fairly good agreement was found between the observed and theoretical bond length and bond angle values for the complex (1) and (2). The *in vitro* antioxidant potential of the complexes was investigated by DPPH, ferrous ion chelation, ferric ion reducing, total antioxidant and hydroxyl free radical scavenging assays. The nature of the tin bonded R groups has apparently a significant impact on the antioxidant activity of the complexes. Molecular docking studies suggest intercalation as possible mode of complex-DNA interactions. Docking studies also confirm that interactions of the two complexes with some active site residues of SARS-CoV-2 nucleocapsid protein and angiotensin-converting enzyme 2 (ACE2) are probable.

1. Introduction

Organotin(IV) carboxylates are well known for their broad spectrum bioactivities including, antibacterial, antifungal, antileishmanial, antituberculosis, and anticancer potential [1–7]. The high charge density and ability of tin to expand its coordination sphere renders these complexes active agents for the interaction with the donor atoms of various biomolecules. An important aspect for its bioactivity is the easy access of the drug molecule to the target cell in preferably unchanged form. Organotin(IV) carboxylates, owing to their hydrolytic stability and concomitant lipophilicity fulfill these criteria. The bioactivity of these complexes is greatly affected by the number and nature of the tin bonded R groups, by the coordination number and the geometry of the complex [1]. Triorganotin(IV) carboxylates can offer better bioactivities than their corresponding diorganotin(IV) analogues. This enhanced bioactivity is due to the increased lipophilicity based on the additional alkyl group in the triorganotin(IV) carboxylates [8,9]. Also triorganotin(IV) species exhibit lower coordination numbers (4 in solution and 5 in solid state) than diorganotin(IV) carboxylates (5/6 in solution and 6 in solid state) [10]. A lower coordination number around the tin ion in triorganotin(IV) derivatives facilitates its interaction with the donor atoms of the biomolecules. In addition to the organotin(IV) moiety, the carboxylate ligand along with its associated functional group(s) appears also quite important for the complex bioactivity [8,11,12]. The coordinated ligand can assist the complex movement through the cellular membranes, affect its hydro/lipophilic character and may affect the electron exchange ability of the complex.

* Corresponding author.
E-mail address: drniaz@awkum.edu.pk (N. Muhammad).

https://doi.org/10.1016/j.molstruc.2021.130190
0022-2860/

The bioactivity of organotin(IV) carboxylate complexes is frequently linked to their ability to interact with the cellular DNA and proteins of the target cells [8]. Such complexes have been repeatedly studied for their antimicrobial and anticancer activities. Studies regarding their antioxidant potentials are, however, rare. Furthermore, scientists and researchers are still searching for an effective and safe antiviral agent, specific to severe acute respiratory syndrome coronavirus 2 (SARS-CoV-2), responsible for causing the coronavirus disease 2019 (COVID-19). Spike (S) protein is the main structural protein of the virus that interacts and binds to the host cell receptors to facilitate its entry into the cells [13,14]. The human angiotensin-converting enzyme 2(ACE2) has been identified by X-ray crystallographic investigations as the specific receptor for the spike (S) protein's receptor binding domain (RBD) of SARS-CoV [15–17]. Along with the synthesis of new potential drugs, two presently pursued important strategies for finding suitable compounds comprise known drug repurposing and computational docking analyses. The potential of organotin(IV) compounds in this regard has yet to be explored against COVID-19 disease.

Considering the bioactivities of organotin(IV) carboxylates and the urgent need for an anti- SARS-CoV-2 drug, we have investigated two newly synthesized triorganotin(IV)−2-chlorphenyl ethanoates for their *in vitro* antioxidant potential, for their in silico DNA binding and their SARS-CoV-2 interaction abilities.

2. Experimental

2.1. Materials and physical measurements

Tri-*n*–butyl–, trimethyltin(IV) chloride and 2-chlorophenyl acetic acid, DPPH, ethanol, ascorbic acid, o-phenantroline, ferrous sulphite, tris-HCl buffer, ethylenediaminetetraacetic acid, ferric chloride, sulphuric acid, potassium monophosphate, potassium diphosphate, ammonium molybdate and hydrogen peroxide were purchased from the commercial suppliers and used as such without any further purification. Chloroform, used as a solvent, was dried according to a reported procedure [18]. A Gallenkamp (UK) electrothermal melting point apparatus was used for the melting point determinations. A Lenco CHNS 932 apparatus was used for the elemental analyses. A Nicolet-6700 FTIR spectrophotometer, Thermoscientific, USA, using attenuated total reflectance (ATR) technique was used to record the FT-IR spectra (4000–400 cm^{-1}). The NMR spectra were obtained at room temperature on a Bruker Advance Digital 300 MHz NMR spectrometer (^{1}H and ^{13}C) and Mercury Plus-400 NMR spectrometer (^{119}Sn). The chemical shifts were provided in ppm relative to Me_4Si and Me_4Sn in $CDCl_3$ solvent.

2.2. Syntheses

2.2.1. Synthesis of sodium-2-chloropenylethanoate (NaL)

The sodium carboxylate salt, NaL was made by the dropwise addition of 2-chlorophenyl acetic acid dissolved in methanol (15 mL) to the aqueous $NaHCO_3$ solution (15 mL) in equimolar ratio. The reaction mixture was stirred at 40 °C for an hour. A white solid obtained after rotary evaporation of the solvent was dried under vacuum.

2.2.2. Tri-n-butyltin(IV) 2-chlorophenylethanoate ***(1)***

Complex **1** was synthesized by mixing equimolar amounts of sodium-2-chlorphenylethanoate (0.963 g, 5 mmol) and tri-*n*-butyltin(IV) chloride (1.628 g, 5 mmol) in dry chloroform followed by heating under reflux condition for 8 hrs as shown in scheme 1. The turbid mixture was left overnight and the precipitated sodium chloride was removed by filtration. The filtrate was rotary evaporated to obtain a solid product which was recrystallized from a chloroform and *n*-hexane mixture (4:1). Yield: 85%. M.p. 57 °C. Anal. Cal. (%) for $C_{20}H_{33}ClO_2Sn$: C, 52.26; H, 7.24. Found (%): C, 52.24; H, 7.25. IR (cm^{-1}): 1560 $\nu(COO)_{asym}$, 1388 $\nu(COO)_{sym}$, 172 $\Delta\nu$, 539, ν(Sn-C); 474 ν(Sn-O). ^{1}H NMR ($CDCl_3$, ppm): 3.77 (s, H2, 2H); 7.39–7.17 (m, Ar-H, 4H); 1.61 (t, Hα, 6H); 1.39–1.25 (m, Hβ,γ, 12H); 0.91 (t, Hδ, 9H). ^{13}C NMR ($CDCl_3$, ppm), $^{n}J[(^{119/117}Sn, ^{13}C)$, Hz]: 175.6 (C-1), 39.9 (C-2), 134.6, 134.3, 131.4, 129.4, 128.1, 126.7 (Ar-C), 16.5 {(C-α), [353/337]}, 27.8 {(C-β), [20]}, 27.02 {(C-γ), [64/62]}, 13.7 (C-δ). ^{119}Sn-NMR ($CDCl_3$, ppm): 110.1.

2.2.3. Trimethyltin(IV) 2-chlorophenylethanoate ***(2)***

Complex **2** was synthesized and recrystallized in the same manner as complex **1**. Sodium-2-chlorphenylethanoate (0.963 g, 5 mmol), trimethyltin(IV) chloride (0.996 g, 5 mmol).Yield: 81%. M.p. 138 °C. Anal. Cal. (%) for $C_{11}H_{15}ClO_2Sn$: C, 39.63; H, 4.53. Found (%): C, 39.61; H, 4.52. IR (cm^{-1}): 1565 $\nu(COO)_{asym}$, 1385 $\nu(COO)_{sym}$, 180 $\Delta\nu$, 547 ν(Sn-C); 469 ν(Sn-O). ^{1}H NMR ($CDCl_3$, ppm), $^{2}J[(^{119/117}Sn, ^{1}H)$, Hz]: 3.78 (s, H2, 2H); 7.40–7.19 (m, Ar-H, 4H); 0.58 {(s, Hα, 9H), [58/56]}. ^{13}C NMR ($CDCl_3$, ppm), $^{1}J[(^{119/117}Sn, ^{13}C)$, Hz]: 176.0 (C-1), 39.9 (C-2), 134.6, 134.0, 131.4, 129.4, 128.30, 126.8 (Ar-C), −2.3 {(C-α), [394/377]}. ^{119}Sn-NMR ($CDCl_3$, ppm): 139.0.

2.3. X-ray single crystal analysis

Appropriately sized single crystals of the synthesized complexes **1** and **2** were immerged in paraffin oil and mounted on a glass fiber for the analyses. The data were obtained with a STOE IPDS 2 T diffractometer (graphite-monochromated Mo Kα radiation, $\lambda = 0.71073$ Å) at 293 K. Direct methods (SHELXS-2013) were used to solve the structures and refinement against all data was done by using full-matrix least-squares methods on F^2 (SHELXL-13) [19]. Anisotropic displacement parameters were used for the refinement of all non-H atoms. The refinement of H atoms was carried out isotropically on calculated positions using a riding model with their U_{iso}values constrained to 1.5 U_{eq} of their pivot atoms for the terminal sp^3 C-atoms and 1.2 times for all other C-atoms. The n–butyl chains of all organic substituents are heavily disordered. This was modeled with two occupation sites for all involved atoms using SADI, SIMU and DELU constraints. The respective ellipsoids remain rather large, though, as the alkyl chains show overall extensive movement in the crystal lattice without being controlled by any form of hydrogen bonding. One chlorine substituted phenyl-ring in the asymmetric unit is also disordered over two positions by a flipping of the phenyl ring (180° rotation). No constraints were used in the modeling of this disorder.

Crystallographic data for the two structures reported here were deposited with the Cambridge Crystallographic Data center, CCDC, 12 Union Road, Cambridge CB21EZ, UK. The data can be obtained free of charge on quoting the depository numbers 1,994,352 (**1**) and 1,994,435 (**2**) by FAX (+44–1223–336–033) email (deposit@ccdc.cam.ac.uk) or their web interface (at http://www.ccdc.cam.ac.uk)

2.4. Computational methods

2.4.1. Molecular docking studies

The three dimensional (3D) structures of the synthesized complexes were drawn with the Molecular Operating Environment (MOE-2016) software [20]. The crystal structures of the salmon sperm-DNA, (PDB id: 1BNA), angiotensin-converting enzyme 2 (PDB code; 1R42), spike protein of SARS-CoV-2 (PDB id: 6CS2) and nucleocapsid protein of SARS-CoV-2 (PDB id: 6M3M) were retrieved from the protein databank [www.rcsb.org/pdb]. Prior to molecular docking, all water molecules were removed from the retrieved crystal structures using the Molecular Operating Environ-

ment software (www.chemcomp.com). The 3D protonation and energy minimization of all the retrieved crystal structures was carried out using the MOE software with its default parameters. The macromolecules were allowed to dock to the synthesized complexes using MOE with default parameters *i.e.*, placement: Triangle Matcher, rescoring: London dG for DNA and GBVI/WSA dG for proteins. For each complex ten conformations were generated. The top-ranked conformation of each compound was used for further analysis.

2.4.2. DFT calculations

The DFT studies of the synthesized complexes **1** and **2** were performed with the Gaussian 09 software [21]. The molecular geometry visualization and respective graphics were carried out and generated with Gauss view 5.0 [22]. The geometries of both complexes (1 and 2) were fully optimized in the gaseous phase by using density functional theory at B3LYP/LANL2DZ level. Two separate basis sets were employed for the calculation, 6–31G(d, p) was employed for the C, H, O, Cl, and Lanl2DZ was employed for Sn [23–25]. From the highest occupied molecular orbital (HOMO) and lowest unoccupied molecular orbital (LUMO), the frontier molecular orbitals energy band gap (E_g) and global reactivity parameters such as chemical hardness, softness, electronegativity and chemical potential were calculated with Koopman's theorem at the same level of theory as used for the optimization [26]. Molecular electrostatic potential (MEP) surfaces were analyzed to identify electron-rich and -deficient regions in the synthesized complexes.

2.5. Antioxidant activities

The synthesized complexes were studied for their *in vitro* antioxidant potential by different assays using a UV-Visible Spectrophotometer.

2.5.1. DPPH radical scavenging assay

The synthesized complexes **1** and **2** were tested for their *in vitro* DPPH radical scavenging assay according to a reported method [27]. Different concentrations (12.5, 25, 50, 100 and 200 µM) of the test complexes were mixed with 1 mL ethanolic solution of DPPH (300 µM). The mixture solutions were shaken and incubated in the dark for 30 min at room temperature. The subsequent decrease in absorbance was measured at 518 nm. Ascorbic acid at the same concentrations was used as a positive control to determine the maximal decrease in DPPH absorbance. The experiments were carried out in triplicates.

2.5.2. Ferrous ion-chelating assay

The ferrous ion chelating abilities of the synthesized complexes **1** and **2** were determined with the o-phenantroline procedure based on the formation of an iron(II)-o-phenanthroline complex [28]. A 3.0 mL distilled water solution containing varying concentrations of synthesized complexes (12.5, 25, 50, 100 and 200 µM), 0.1 mL of 9 mM o-phenanthroline, 0.2 mL of 3.6 mM ferrous sulfate and 0.3 mL of 100 mM tris-HCl buffer (pH = 7.4) were incubated for a period of 10 min at room temperature. The absorbance of the solutions was measured at 510 nm. Ethylenediaminetetraacetic acid (EDTA) was used as a reference.

2.5.3. Ferric-reducing antioxidant power assay

The ferric ion reduction potentials of the synthesized complexes **1** and **2** were determined with the ortho-phenanthroline method [29]. Different concentrations (12.5, 25, 50, 100 and 200 µM) of the synthesized complexes **1** and **2** were added to a solution containing 200 µL of 4.5 mM *o*-phenanthroline, 0.15 mL of 0.2 M tris-HCl buffer (pH = 7.4), 400 µL of 1.8 mM ferric chloride. The solution was diluted with distilled pure water up to 3000 µL in a test tube. The reaction mixtures were shaken vigorously. After 10 min the change in the absorbance values was measured at 510 nm. Vitamin-C was used as a reference.

2.5.4. Total antioxidant capacity assay

The total antioxidant activities of the synthesized complexes **1** and **2** were determined with the phosphomolybdenum method as described earlier [30]. Different concentrations (12.5, 25, 50, 100 and 200 µM) of the synthesized complexes **1** and **2** were mixed with reagent solution containing 700 µL of 0.6 M sulfuric acid, 1000 µL of 28 mM potassium monophosphate and diphsophate, 1.0 mM ammonium molybdate and were diluted up to 3 mL with distilled water. The reaction tubes, covered with silver foil, were incubated for 90 mins in a boiling water bath at 95 °C. The reaction mixtures were cooled down to room temperature and the change in absorbance was measured at 695 nm by UV/VIS spectroscopy. Vitamin-C was used as a reference.

2.5.5. Hydroxyl free radical scavenging assay

The hydroxyl radial scavenging ability of the synthesized complexes **1** and **2** was tested using the Fenton reaction [31]. Varying concentrations (12.5, 25, 50, 100 and 200 µM) of the synthesized complexes, 0.1 mL of 7.5 mM o-phenanthroline, 0.5 mL of 0.2 M phosphate buffer (pH 6.6), 0.1 mL of 7.5 mM ferrous sulfate and 0.1 mL of H_2O_2 (0.1%) were mixed and diluted up to 3 mL with distilled water. The reaction mixtures were incubated at room temperature for 30 min. The absorbance of the mixture solution was measured at 510 nm. The reaction mixture without synthesized complexes was used as a control and the one without complexes and H_2O_2 as a blank.

3. Results and discussion

3.1. Synthesis

Organotin(IV) carboxylates were synthesized by the reaction of R_3SnCl {R = C_4H_9 (**1**) and CH_3 (**2**)} with sodium-2-chlorophenylethanoate (1:1) in dry chloroform. The reaction mixtures were refluxed for 8 h. The complexes were obtained in good yields (> 80%). They are white solids and soluble in toluene, chloroform and DMSO.

3.2. FT-IR spectroscopy

Comparison of the FT-IR spectra of the free ligand acid **HL** with the synthesized complexes **1** and **2** confirmed the formation of the carboxylate complexes (figures S1–3). The most explicit feature of the complexes spectra is the absence of a broad band (3400–2400 cm^{-1}) owing to the OH vibration of the COOH moiety [32]. The presence of weak bands in the spectra of complexes **1** and **2** at 474 cm^{-1} and 469 cm^{-1}, respectively, further support their formation [11]. In addition, the strong bands owing to C=O (1706 cm^{-1}) and C–O (1233 cm^{-1}) vibrations in the free ligand acid **HL** were also absent in the spectra of both complexes. These bands were replaced by antisymmetric (1560, 1565 cm^{-1}) and symmetric vibrations (1388, 1385 cm^{-1}) of the COO moiety in complexes **1** and **2**, respectively. The difference (Δv) of antisymmetric and symmetric COO vibrations in complexes **1** (172) and **2** (180) indicated bridging bidentate coordination modes of the carboxylate ligands [11]. The IR spectral findings are well supported by the X-ray single crystal data of complexes **1** and **2**.

3.3. NMR spectroscopy

The solution state structural characterization by ^1H and ^{13}C NMR spectra for the synthesized complexes was performed in

deuterated chloroform. The ^{1}H NMR spectra of the synthesized complexes exhibit no peaks in the deshielded region above 9 ppm. This observation agrees with the carboxylate ligands being deprotonated in the synthesized complexes **1** and **2** [1]. Three types of signals owing to the tin bonded alkyl protons (below 2 ppm), ligand methylene protons (at 3.77 ppm) and ligand aryl protons (7.5–7.00) were observed with expected multiplicities and intensity patterns in the ^{1}H NMR spectra of the synthesized complexes. In the ^{1}H NMR of complex **1** a triplet (Hα), multiplet (Hβ,γ) and triplet pattern was observed for the tin bonded $-CH_2-CH_2-CH_2-CH_3$ skeleton in the shielded part of the spectrum [1]. The ^{1}H NMR spectrum of the complex **2** was simple and more informative compared to the complex **1**. The tin bonded methyl protons appeared as singlet at 0.58 ppm with well resolved satellites giving a coupling constant ^{2}J[($^{119/117}$Sn,1H), Hz] of 58/56 Hz. This coupling constant value suggested a tetrahedral geometry for the tin atom in solution [1]. The argument was further supported by the Me-Sn-Me angle calculation (111.0°) using the Lockhart equation, $\theta = 0.0161\ [2\ J]^2 - 1.32\ [2\ J] + 133.4$ [33].

In the ^{13}C NMR spectra of the synthesized complexes the signals due to different carbon atoms were found in the expected regions. The peaks were assigned by comparing the spectra with previously reported similar complexes [11]. The coordination number and geometry around tin in the synthesized complexes **1** and **2** were derived from the ^{1}J[($^{119/117}$Sn, ^{13}C) coupling constant values. The calculated values are 353/337 and 394/377 Hz thus suggesting four coordinated tetrahedral tin centers in the synthesized complexes **1** and **2**, respectively [10]. The calculated angles from the ^{1}J[($^{119/117}$Sn, ^{13}C) values were found to be almost ideal for tetrahedral geometry with 107.7° and 111.3° for complexes **1** and **2**, respectively, furthermore the ^{119}Sn NMR signals also supported typical four-coordinated tin [10,11].The absence of any extra peak in the spectra emphasizes the very high purity of the synthesized complexes.

3.4. Crystal structure description

The two organotin(IV) derivatives (**1** and **2**) of 2-chlorophenylacetic acid shown in Figs. 1(a) and 2(a), respectively, crystallized in the monoclinic crystal system. The corresponding crystal data is shown in Table 1 and important bond lengths and angles of both the complexes are shown in Tables 2 and 3, respectively. The crystal packing diagrams reveal four sub units of coordination polymers with μ-K,$^{1}K^{1}$ bidentate 2-chlorophenylacetate ligands. The supramolecular structures of the single units of complexes **1** and **2** are shown in Figs. 1(b), 1(c) and Fig. 2(b), respectively.

The asymmetric units of the coordination polymers in both complexes include two types of tin atoms with distorted trigonal bipyramidal geometries which is also confirmed by the respective τ values ($\tau = \beta$-α/60 where β and α are the two largest basal angles) [34]. For penta-coordinated Sn with perfect trigonal-bipyramidal geometry the τ value is one whereas a value of zero corresponds to a perfect square-pyramidal structure. The calculated τ values were found to be 0.828Sn1/0.823Sn2 and 0.862Sn1/0.886Sn2 for complexes **1** and **2**, respectively, indicating slightly distorted trigonal-bipyramidal geometries around the tin atoms. The values, furthermore, reflect a stronger distortion for complex **1** relative to complex **2**. In complex **1** bulky *n*–butyl groups and the concomitant mild steric strain result in more distortion compared to the complex **2** with much smaller methyl substituents.

The apparent distortion in the geometries is also reflected in the equatorial Sn–C bond lengths as summarized in Tables 2 and 3 for the complexes **1** and **2**, respectively. The Sn–C bond lengths in complex **1** are shorter while those in complex **2** are comparable to the typical Sn–C bond lengths in structurally related trigonal bipyramidal organotin(IV) complexes [35,36]. The axial O–Sn–O angles in complex **1** {O4^{ii}–Sn1–O1 = 172.20 (16)° and O2–Sn2–O3 = 173.18 (15)°} show more distortion compared to the same angles in complex **2** {O4–Sn1–O2 = 174.81 (16)° and O1–Sn2–O3 = 178.82 (18)°} from the ideal trigonal bipyramidal value of 180° Also, in complex **1**, O–Sn–O angles show only minor differences **{**–0.98°**}** compared to complex **2,** where the O–Sn–O angles differ for the two Me_3SnO_2 moieties of the same unit by –4.01° In complex **2**, the smaller methyl groups allow a closer packing of the coordination polymers, thereby facilitating interactions of the 2–chloro substituent with the O–Sn–O moieties which results in a greater difference in their angle values. For the same reason the sum of equatorial angles {C–Sn1–C = 358.4°, C–Sn2–

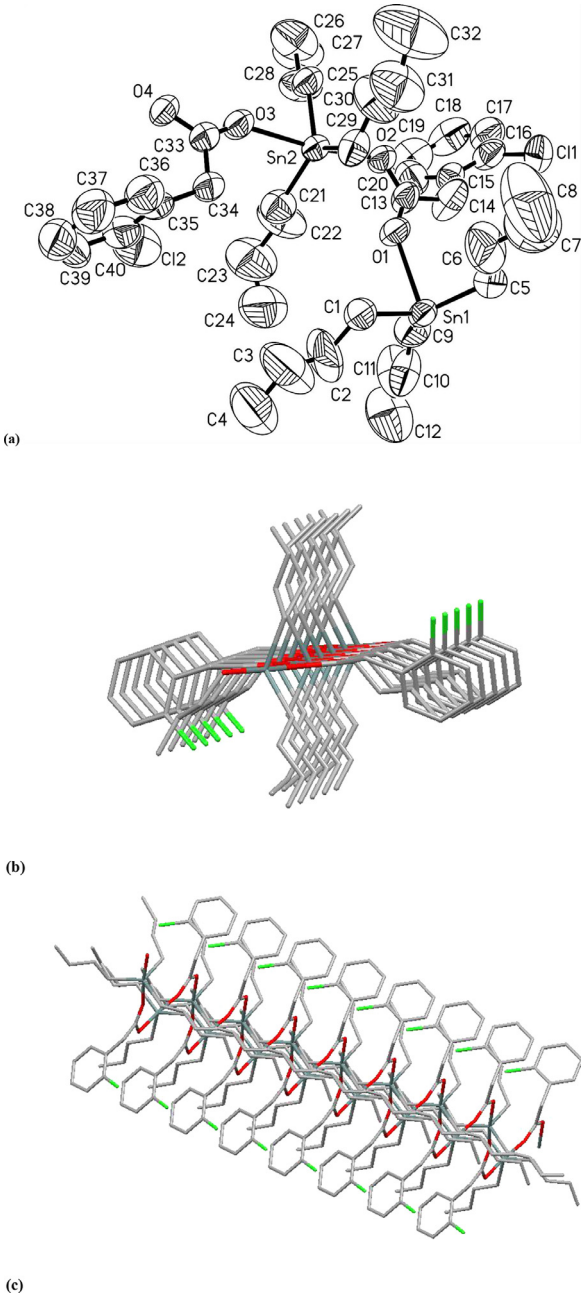

Fig. 1. (a) The asymmetric unit of the molecular structure of complex **1**; (b) polymeric chain protruding along the crystallographic a axis.; and (c) 3D view of the coordination polymers of complex **1**. Hydrogen atoms are omitted for clarity.

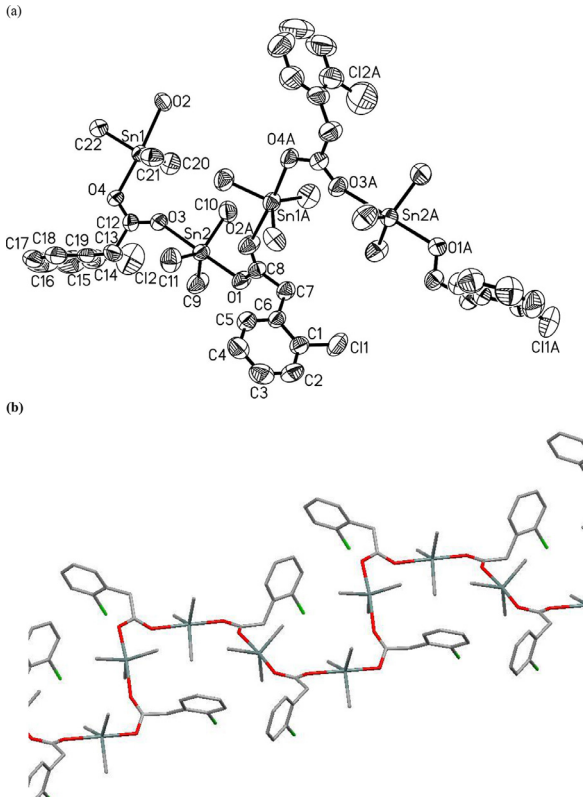

Fig. 2. (a) The molecular structure of complex **2** and (b) coordination polymer formed by complex **2**. Hydrogen atoms are omitted for the clarity.

Table 1
Crystal and refinement data of complexes **1** and **2**.

Complex	**1**	**2**
Empirical formula	$C_{40}H_{66}Cl_2O_4Sn_2$	$C_{22}H_{30}Cl_2O_4Sn_2$
Formula mass	919.20	666.74
Temperature (K)	293	293
Wavelength (Å)	0.71073	0.71073
Crystal system, space group	Monoclinic, $P2_1/c$	Monoclinic, $P2_1/n$
Unit cell dimensions (Å)	a = 10.405 (2), b = 21.041 (4), c = 22.830 (6), β = 109.36 (3)°	a = 7.0555 (14), b = 28.314 (6), c = 13.607 (3) β = 92.78 (3)°
Z, Volume (Å^3)	4, 4716 (2)	4, 2715.0 (9)
Crystal size (mm)	0.49 × 0.21 × 0.17	0.10 × 0.09 × 0.09
Calculated density (Mg m^{-3})	1.295	1.631
Absorption coefficient (mm^{-1})	1.21	2.06
F(000)	1888	1312
Θ range for data collection	6.1–45.5°	6.2–48.3°
Limiting indices	h = −11→11, k = −22→22, l = −24→24	h = −7→7, k = −31→31, l = −15→15
Measured reflections	28,660	15,778
Independent reflections	6189	4031
Reflections with $I > 2\sigma(I)$	2874	2606
R_{int}	0.071	0.068
Refinement method	Full-matrix least-squares on F^2	Full-matrix least-squares on F^2
Data/restraints/ parameters	6189/283/501	4031/0/271
$R[F^2 > 2\sigma(F^2)]$	0.037	0.037
τ-values	0.828 (Sn1), 0.823 (Sn2)	0.862 (Sn1), 0.886 (Sn2)

C = 358.9°} in complex **2** is more distorted than complex **1** {C–Sn1–C = 359°, C–Sn2–C = 359.3°}.

The Sn–O distances for Sn1….O3 = 3.077 Å and Sn2….O2 = 3.125 Å in complex **2**, though longer than typical Sn–O covalent bonds, are still shorter than the reported sum of van der Waals radii of Sn and O (3.7 Å) [37]. Complex **2** may be assigned distorted octahedral geometries if these bonds are not neglected and the respective oxygen atoms are then considered as being coordinated to both tin ions simultaneously. In complex **1** the same bond lengths due to the presence of the bulky *n*–butyl substituents is exceeding 4 Å which is longer than the sum of van der Waals radii of Sn and O and a respective interaction can be excluded here.

3.5. DFT calculations

3.5.1. DFT optimized geometries

The geometries of the synthesized complexes **1** and **2** were fully optimized in the gas phase with density functional theory (DFT) methods at the B3LYP/LANL2DZ level and are shown in figures S4–6 in the supplementary data. The selected bond lengths and bond

Table 2
Selected bond lengths (Å) and bond angles (°) of complex **1**[a].

Moiety	Bond lengths (Exp.)	Bond lengths (Calc.)	Moiety	Bond lengths (Exp.)	Bond lengths (Calc.)
C21-Sn2	2.071 (9)	2.14	C1-Sn1	2.102 (7)	–
C25-Sn2	2.108 (7)	2.151	C5-Sn1	2.115 (8)	–
C29-Sn2	2.05 (4)	2.152	C9-Sn1	2.080 (10)	–
O2-Sn2	2.187 (4)	2.15	O1-Sn1	2.426 (4)	–
O3-Sn2	2.426 (5)	2.056	O4ii- Sn1	2.154 (4)	–
C33-O3	1.240 (8)	1.31	C13-O1	1.237 (7)	–
C33-O4	1.262 (7)	1.22	C13-O2	1.265 (7)	–
C40-Cl2	1.545	1.76			
Moiety	Bond angles (Exp.)	Bond angles (Calc.)	Moiety	Bond angles (Exp.)	Bond angles (Calc.)
C21-Sn2-C25	118.3 (4)	113.6	C30-C29-Sn2	116	115.95
C21-Sn2-C29	123.5 (7)	117.69	O3-C33-C34	116.9	116.16
C25-Sn2-C29	117.5 (6)	113.6	O4-C33-C34	120.5	122.78
O2-Sn2-O3	173.18 (15)	176.43	O3-C33-O4	122.6	122.7
C25-Sn2-O3	84.3	96.3	C9-Sn1-C1	118.9 (4)	–
C21-Sn2-O3	86.5	105.6	C9-Sn1-C5	122.5 (4)	–
C29-Sn2-O3	90.8	106.43	C1-Sn1-C5	117.6 (4)	–
C22-C21-Sn2	122.9	115.93	O4ii-Sn1-O1	172.20 (16)	–
C26-C25-Sn2	116.7	115.53			–

[a] = dash indicates value not calculated(i) x − 1, y, z; (ii) x + 1, y, z.

Table 3
Selected bond lengths (Å) and bond angles (°) of complex **2**[a].

Moiety	Bond lengths (Exp.)	Bond length (Calc.)	Moiety	Bond lengths (Exp.)	Bond length (Calc.)
C9-Sn2	2.123 (8)	2.137	C20-Sn1	2.093 (8)	–
C10-Sn2	2.111 (7)	2.131	C21-Sn1	2.103 (7)	–
C11-Sn2	2.102 (8)	2.133	C22-Sn1	2.117 (7)	–
O1-Sn2	2.195 (4)	2.047	O2-Sn1	2.433 (5)	–
O3-Sn2	2.399 (4)	2.43	O4-Sn1	2.194 (4)	–
C8-O2^{i}	1.229 (8)	1.227	C12-O3	1.235 (8)	–
C8-O1	1.278 (8)	1.31	C12-O4	1.274 (8)	–
Moiety	Bond angles (Exp.)	Bond angles (Calc.)	Moiety	Bond angles (Exp.)	Bond angles (Calc.)
C10-Sn2-C9	114.1 (4)	112.646	O2-C8-O1	122.8	123.123
C11-Sn2-C10	125.7 (4)	117.660	C9-Sn2-O1	90.3	96.8
C11-Sn2-C9	119.1 (4)	113.123	O1-C8-C7	115.8	115.8
O1-Sn2-O3	178.82 (18)	177.6	C20-Sn1-C21	123.1 (3)	–
C10-Sn2-O1	95.2	107.6	C20-Sn1-C22	119.5 (3)	–
C11-Sn2-O1	94.6	106.8	C21-Sn1-C22	115.8 (3)	–
C8-O1-Sn2	118.6	117.292	O4-Sn1-O2	174.81 (16)	–
O2-C8-C7	121.3	121.014			

[a] = dash indicates value not calculated(i) $x + 1/2, -y + 1/2, z + 1/2$; (ii) $x - 1/2, -y + 1/2, z - 1/2$.

angles in the optimized complexes geometries were calculated using a combination of two basis sets. For the four lighter atoms (C, H, O, Cl) the 6–31G(d, p) basis set and for the Sn atom the LANL2DZ basis set were used. Theoretically predicted parameters have shown a fairly good agreement with the corresponding experimental data for the complexes **1** and **2** as shown in Tables 2 and 3, respectively. Experimental data revealed polymeric chain structures for the complexes **1** and **2** including two different types of tin atoms in the solid state. In the theoretical approach, bond lengths and bond angles were calculated for only one type of tin atom and in a gaseous phase optimized form. For these reasons some deviations can be observed in the experimental and theoretically calculated data. In complex **1**, the experimental and theoretically calculated bond lengths have maximum and minimum bond length differences of 0.366 Å and 0.037 Å in the Sn2-O3 and Sn2-O2 bonds, respectively. Also the experimental and theoretical calculated bond angles have maximum and minimum bond angle differences of 19.1° and 0.05° for the C21-Sn2-O3 and C30-C29-Sn2 angles, respectively. The comparatively large difference of 19.1° in the bond angle C21-Sn2-O3 could be assigned to the aforementioned factors and is also due to the presence of intermolecular interactions in the solid crystalline form. In complex **2**, the experimental and theoretically calculated distances have maximum and minimum bond length differences of 0.148 Å and 0.002 Å for the Sn2-O1 and C8-O2^{i} bonds, respectively. Similarly, the experimental and theoretical calculated bond angles have maximum and minimum bond angle differences of 12.4° and 0° for the C10-Sn2-O1 and O1-C8-C7 angles, respectively.

3.5.2. Quantum Chemical calculations

In order to better understand the stability and electronic properties of the synthesized complexes **1** and **2**, frontier molecular orbital calculations were carried out with DFT methods at the B3lyp/Lanl2DZ level of theory. The energies of the highest occupied molecular orbital (HOMO) and of the lowest unoccupied molecular orbital energy (LUMO) and the respective energy band gap play an important role in estimating the physical and electronic properties of the molecules.

The HOMO represents the electron rich and the LUMO comprises the electron deficient region of the molecule showing electron donating and accepting abilities, respectively [38,39]. The frontier molecular orbitals (HOMO and LUMO) of the synthesized complexes are shown in Table 4. In both the synthesized complexes the HOMO and LUMO are predominantly located on the carboxylate ligand. The HOMO resides on the benzene ring, chlorine atom and carboxyl (COO) group, while the LUMO is mainly located on the benzene ring with a minor extension towards the chlorine and the carboxyl (COO) group of the coordinated ligand. The energy gaps (E_g) between HOMO and LUMO play an important role in the structural and kinetic stability of a molecule [40–42]. A smaller or larger HOMO-LUMO energy gap entails a more reactive or more stable nature of the molecule, respectively [42,43]. The calculated HOMO and LUMO energy gaps of complexes **1** and **2** are similar 6.1005 and 6.25094 eV, respectively (figures S7 and S8). The calculated values reflect a comparably good kinetic stability of the complexes [42,43].

The HOMO-LUMO energies were further used to calculate the global reactivity parameters such as the electrophilicity index (ω), electronegativity (χ), chemical potential (μ), ionization potential (I), electron affinity (A), chemical hardness (η) and global softness (S) by using the following equations [44] and the data are displayed in Fig. 3(a).

$$I = -E_{HUMO} \tag{1}$$

$$A = -E_{LUMO} \tag{2}$$

$$Eg = E_{LUMO} - E_{HUMO} \tag{3}$$

$$\eta = \frac{I - A}{2} = \frac{E_{LUMO} - E_{HOMO}}{2} \tag{4}$$

$$\chi = \frac{(I + A)}{2} = \frac{-(E_{LUMO} + E_{HOMO})}{2} \tag{5}$$

$$\mu = \frac{-(I + A)}{2} = \frac{(E_{LUMO} + E_{HOMO})}{2} \tag{6}$$

$$\sigma = \frac{1}{\eta} \tag{7}$$

The global reactivity parameters as shown for the complexes **1** and **2** in Fig. 3(a) are useful descriptors in defining polarizability, the electro/nucleophilic nature and chemical reactivity of a molecule. These parameters give a theoretical insight in the chemical and redox nature of a molecule and facilitate predicting the characteristics of its interaction with biomolecules.

A molecule with a small frontier orbital gap (Eg), lower global hardness (resistance to charge transfer), higher global softness (ease of charge transfer) and a higher electrophilicity index acts as

Table 4
HOMO and LUMO surfaces of the complexes **1** and **2**.

Comp.	HOMO	LUMO
1	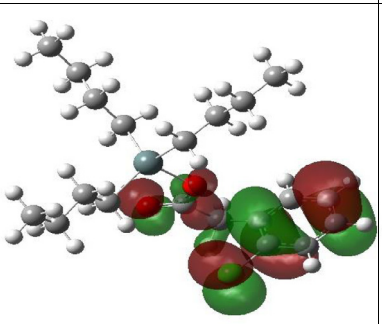	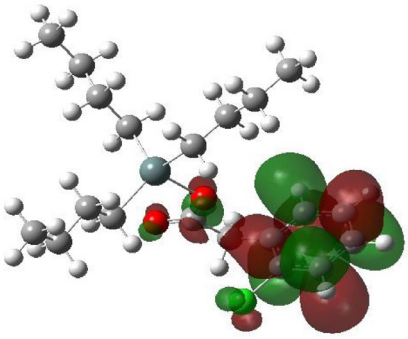
2	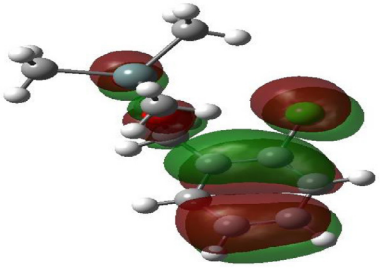	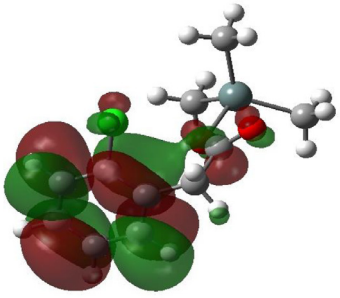

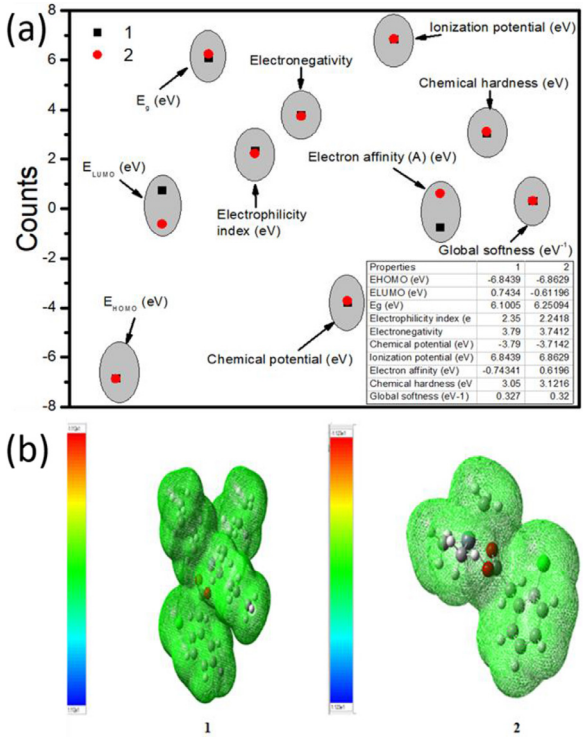

Fig. 3. **(a)** Global reactivity parameters of complexes **1** and **2**, the inset shows numerical data for different parameters. **(b)** Molecular Electrostatic Potential surfaces of complexes **1** and **2**.

a soft, more polarizable and reactive molecule [45]. In the present study lower frontier orbital gap and global hardness values and higher global softness and electrophilicity index values of complex **1** makes it more soft, polarizable and reactive compared to complex **2** for the electron transfer reactions [45]. The absolute electronegativity (χ) value (an indicator for the acidic/basic behavior of a molecule) is slightly higher for complex **1** than for complex **2.** This observation suggests a more acidic character for complex **1**. Further, the larger values of the chemical potentials for complex **1** and complex **2** (with **1** > **2**) show that the energy of the complexes is more sensitive towards a redox transformation compared to the previously reported complexes [45]. The calculated global reactivity parameters suggest that the synthesized complexes **1** and **2** can potentially show antioxidant and biological activity owing to their softer, more polarizable and better charge transfer ability compared to the previously reported organotin(IV) complexes [45,46].

3.5.3. Molecular electrostatic potential (MEP) surface analysis

Molecular electrostatic potential (MEP) surfaces provide graphical information about the relative polarity of a molecule. The MEP surfaces of the synthesized complexes mapped with electrostatic potential dispersion (−1.112–1.112 esu for **1** and −1.123–1.23 esu for **2**) are shown in Fig. 3b. The narrow electrostatic potential dispersion range and absence of red or blue color on the entire MEP surface emphasize a rather neutral nature of the synthesized complexes [47]. This might be beneficial in a sense that these molecules are not expected to interfere strongly with ion channels or transporters in cells which, *inter alia*, is associated with the typical toxicity of organotin compounds.

3.6. Molecular docking study

3.6.1. DNA interaction

Molecular docking studies were performed to identify the theoretical binding interactions of the synthesized complexes **1** and **2** with DNA. Usually for drug-DNA interaction the salmon sperm DNA is used due to its high binding affinity with drug molecules and stability of drug-DNA complex during UV-absorption analysis, carried out for binding constant calculations. Complex **1** (dock-

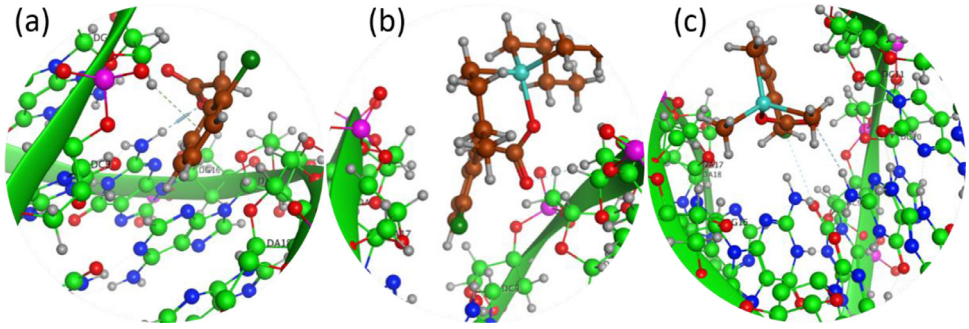

Fig. 4. Molecular docked structure of (a) free ligand acid (**HL**) with DNA (b) complex **1** with DNA and (c) complex **2** with DNA.

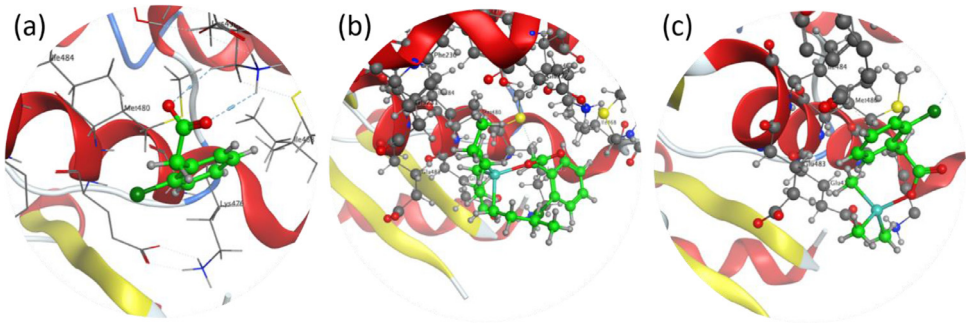

Fig. 5. Molecular docked structure of (a) free ligand acid (**HL**) (b) complex **1** and (c) complex **2** with angiotensin-converting enzyme 2.

ing score = −7.4576) showed a polar interaction with the active residues (DC 11) of the DNA as shown in Fig. 4(b). Complex **2** (docking score = −7.2043) showed two polar interactions with the active site residues (DC 9, DG 10) of the DNA as shown in Fig. 4(c). Free acid ligand **HL** (docking score = −7.0978) showed two polar interactions with the DNA active residues (DG 16 and DG 10) as shown in Fig. 4(a). The docking scores imply an activity order **1** > **2** > **HL** which supports the presumption that complexation could increase the DNA binding efficiency of the acid ligand. Also keeping all other factors (carboxylate ligand, number of alkyl groups, geometry around tin atom) the same, the nature of the alkyl group can affect the DNA binding potential of the synthesized complexes.

3.6.2. Corona virus SARS-CoV-2 proteins and angiotensin converting enzyme 2 docking

Molecular docking studies were also performed to theoretically identify potential interactions of the acid ligand **HL** and the synthesized complexes (**1** and **2**) with the SARS-Co-2 virus responsible for the most challenging disease Covid-19. For the docking studies, nucleocapsid protein, spike protein (point of interaction with the receptor in the human body) of SARS-CoV-2 virus and angiotensin-converting enzyme 2 (ACE2), a possible host/receptor for the SARS-Co-2 virus [48,49] were chosen. The docking computations revealed some considerable binding interactions of the acid ligand and the synthesized complexes with the angiotensin-converting enzyme 2 (ACE2) and with the nucleocapsid protein of the SARS-CoV-2 virus. However, no sufficiently stable interactions of the compounds with the spike protein were found. Free acid ligand **HL** (docking score = −7.4586) shows two H-acceptor interactions with LYS 458 of the ACE2 receptor as shown in Fig. 5(a). Complex **1** (docking score = −5.8182) exhibits two H-donor interactions with the active side residues MET 462 and MET 480 of the ACE2 receptor as shown in Fig. 5(b). Complex **2** (docking score = −5.4212) engages in two H-donor, π-H interactions with the active site residues GLU 227 and ILE 484 of the ACE2 receptor as shown in Fig. 5(c). Free acid ligand **HL** (docking score = −7.6944) induces three H-acceptor interactions with ARG 108 of the nucleocapsid protein (Fig. 6(a)). Complex **1** (docking score = −9.1386) shows one H-acceptor interaction with the same active site residue ARG 108 in the nucleocapsid protein (Fig. 6(b)). Complex **2** (docking score = −6.9317) on the other hand establishes one H-donor interaction with the active site ALA 157 in the nucleocapsid protein (Fig. 6(c)). The so far observed theoretical interacting abilities of the synthesized complexes, though promising, require further studies including experimental ones to identify a possible/definitive role of the organotin(IV) carboxylates in controlling corona viruses in the future.

3.7. Antioxidant Activities

The complexes were assessed for their antioxidant potential using DPPH, ferrous ion chelation, ferric ion reducing, total antioxidant and hydroxyl free radical scavenging assays. The activities were tested using different concentrations of the synthesized complexes (12.5, 25, 50, 100 and 200 µM) against ascorbic acid (vitamin C) as a standard drug. For the ferrous ion chelation assay EDTA was used as a standard. The activity of the complexes is shown as IC_{50} values in Table 5. Complex **1** with a lower IC_{50} value has shown a better antioxidant potential compared to complex **2** in DPPH, ferric ion reducing and total antioxidant capacity assays. The antioxidant activity can be explained in terms of H/electron transfer from the antioxidant to the free radical under investigation [50]. Complexes **1** and **2** show similar structural behavior regarding the carboxylate ligand, the ligand coordination mode and the geometry around tin (tetrahedral in solution as confirmed by NMR spectroscopy). The only difference between the complexes is the nature of the alkyl chain/group bound to tin. Complex **1** bears bulky butyl groups with more electron donating ability to the tin ion compared to the smaller methyl groups of complex **2**. The electron donation from the butyl groups renders the respective tin a more electron rich species. Also, the bulky butyl groups impair any additional interaction of the C=O group with the tin atom. Therefore, an electron transfer from the free C=O group to the free radical/ion should generally be possible resulting in (bet-

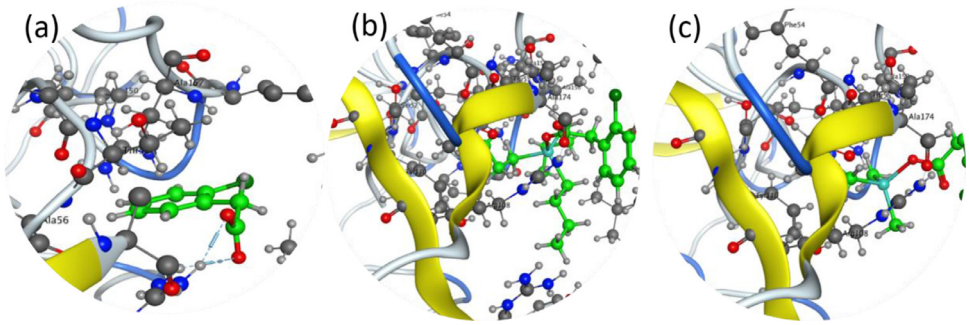

Fig. 6. Molecular docked structure of (a) free ligand acid (**HL**) (b) complex **1** and (c) complex **2** with nucleocapsid protein.

Table 5
IC_{50} values of the synthesized complexes **1** and **2** in different antioxidant assays.

IC_{50} values/μM					
Compounds	DPPH	Ferrou ion Chelation	Ferric ion reducing	Total antioxidant	Hydroxyl free radical
1	58.139 ± 9.74	202.47 ± 8.18	115.90 ± 6.8	133.33 ± 8.87	221.38 ± 8.03
2	116.74 ± 9.51	157.03 ± 9.03	138.77 ± 8.65	139.12 ± 9.07	129.83 ± 10.12
Vit.C	39.20 ± 6.71	–	61.00 ± 10.35	130.00 ± 12.39	87.56 ± 13.90
EDTA	–	116.117 ± 7.83	–	–	–

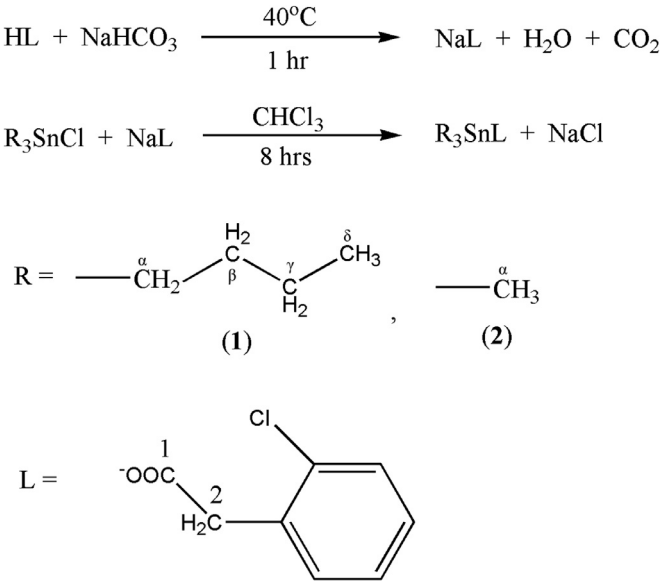

Scheme 1. Synthetic scheme for the synthesis of complexes **1** and **2**.

ter) antioxidant activity [51]. The sterically encumbered structure, hence, makes complex **1** the more active antioxidant compared to complex **2** in these three assays.

Notably, the activity order was reversed in the ferrous ion chelation and hydroxyl free radical scavenging assays. In these protocols complex **2** exhibits lower IC_{50} values and was thereby more active than complex **1**. The activity reversal is attributed to different modes of action in the tested protocols. In complex **2** the smaller methyl groups induce lesser steric hindrance and lower electron donation to the tin. The sterically unsaturated relatively electron deficient tin center in complex **2** might therefore be better suited to act as an efficient direct OH radical scavenger. The smaller methyl group also leaves enough space and flexibility so that the C=O group of the coordinated ligand is free to chelate the iron(II) ions more efficiently making complex **2** the better antioxidant in the respective.

4. Conclusion

Tri-*n*–butyl– {**1**} and trimethyltin(IV) {**2**} complexes of 2-chlorophenylethanoic acid (**HL**) were synthesized by condensation reactions of triorganotin(IV) chlorides with the sodium salt of the acid ligand (NaL) {1:1} in dry chloroform in good yields. Polymeric chain structures comprising penta-coordinated tin centres with bridging carboxylate ligands were confirmed by solid state FT-IR and single crystal analyses. In solution the complexes, (**1, 2**), apparently form four-coordinated tetrahedral tin centres as supported by their respective NMR (^{1}H, ^{13}C and ^{119}Sn) spectra. Smaller frontier molecular orbital gaps and calculated global reactivity parameters imply a softer, more polarizable and more reactive nature of complex **1** compared to **2**. Molecular electrostatic potential surface analyses emphasize a generally neutral nature of the complexes. The antioxidant potential of the complexes was notably affected by the nature of the tin bonded R group. The bulky *n*–butyl group (**1**) improves the electron donating ability of the complex. The smaller methyl group renders complex **2** a better chelating and OH radical attracting agent. Docking studies suggested some complex-DNA (intercalation), complex-nucleocapsid protein of SARS-CoV-2 virus and complex-angiotensin-converting enzyme 2 interactions. The encouraging theoretical interactions of the complexes require further studies of the complexes as possible DNA binders and corona virus inhibitors.

Declaration of Competing Interest

The author(s) declare(s) that there is no conflict of interest regarding the publication of this paper.

CRediT authorship contribution statement

Tariq Ali: Investigation, Validation. **Niaz Muhammad:** Supervision, Resources, Writing – review & editing. **Zafar Ali:** Software. **Abdus Samad:** Software. **Mohammad Ibrahim:** Investigation. **Muhammad Ikram:** Investigation. **Sadia Rehman:** Investigation. **Shaukat Shujah:** Investigation. **Gul Shahzada Khan:** Writing – review & editing. **Abdul Wadood:** Software. **Saqib Ali:** Investigation. **Carola Schulzke:** Investigation.

Acknowledgement

Dr. Niaz Muhammad is thankful to the Higher Education Commission, Pakistan for the financial support through project number 20–3092/R&D/HEC/13 638.

Supplementary materials

Supplementary material associated with this article can be found, in the online version, at doi:10.1016/j.molstruc.2021.130190.

References

[1] N. Muhammad, N.A. Shah, S. Ali, S.N. Elahi, W. Rehman, S. Shujah, M.R. Khan, A. Wadood, M. Ghufran, U. Rashi, Theoretical and experimental *in vitro* antifungal and antitumor activities of organotin(IV) derivatives of 3-(4-nitrophenyl)-2-methylacrylic acid, Pharm. Chem. J. 53 (8) (2019) 689–696.
[2] N. Muhammad, N.A. Shah, S. Ali, S.N. Elahi, W. Rehman, S. Shujah, M.R. Khan, A. Wadood, M. Ghufran, U. Rashid, Theoretical and experimental *in vitro* antifungal and antitumor activities of organotin(IV) derivatives of 3-(4-nitrophenyl)-2-methylacrylic acid, Phosphorus Sulfur Silicon Relat. Elem. 194 (11) (2019) 1067–1073.
[3] M. Sirajuddin, S. Ali, V. McKee, N. Akhtar, S. Andleeb, A. Wadood, Spectroscopic characterizations, structural peculiarities, molecular docking study and evaluation of biological potential of newly designed organotin(IV) carboxylates, J. Photochem. Photobiol. B 197 (2019) 111516.
[4] H. Hussain, N. Bibi, AhmedAl-Harrasi, S. Siddiqi, S. U.Kazmi, Y. Zhang, A. Badshah, Antituberculosis and cytotoxic activities of triorganotin(IV) complexes, Chin. Chem. Lett. 23 (6) (2012) 731–735.
[5] M. Gielen, M. Biesemans, D. Vos, R. Willem, Synthesis, characterization and *in vitro* antitumor activity of di- and triorganotin derivatives of polyoxa- and biologically relevant carboxylic acids, J. Inorg. Biochem. 79 (2000) 139–145.
[6] J. Liu, Y. Lin, M. Liu, S. Wang, Y. Li, X. Liu, L. Tian, Synthesis, structural characterization and cytotoxic activity of triorganotin 5-(salicylideneamino) salicylates, Appl. Organomet. Chem. 33 (3) (2019) e4715.
[7] M. Sirajuddin, S. Ali, V. McKee, S. Zaib, J. Iqbal, Organotin(IV) carboxylate derivatives as a new addition to anticancer and antileishmanial agents: design, physicochemical characterization and interaction with Salmon spermDNA, RSC Adv. 4 (2014) 57505–57521.
[8] C.N. Banti, SK. Hadjikakoua, T. Sismanoglu, N. Hadjiliadis, Anti-proliferative and antitumor activity of organotin(IV) compounds. Anoverview of the last decade and future perspectives, J. Inorg. Biochem. 194 (2019) 114–152.
[9] M. Gielen, M. Bouâlam, A. Meriem, B. Mahieu, M. Biesemans, R. Willem, Dialkyltin derivatives of dicarboxylic acids: synthesis, characterization and *in vitro* antitumor properties, Heteroat. Chem. 3 (1992) 449–452.
[10] N. Muhammad, Zia-ur-Rehman, S. Ali, A. Meetsma, F. Shaheen, Organotin(IV) 4-methoxyphenylethanoates: synthesis, spectroscopic characterization, X-ray structures and *in vitro* anticancer activity against human prostate cell lines (PC-3), Inorganica. Chim. Acta 362 (2009) 2842–2848.
[11] N. Muhammad, Zia-ur-Rehman, S. Shujah, S. Ali, A. Shah, A. Meetsma, Synthesis and structural characterization of monomeric and polymeric supramolecular organotin(IV) 4-chlorophenylethanoates, J. Coord. Chem. 67 (6) (2014) 1110–1120.
[12] T.A. Antonenko, D.B. Shpakovsky, D.A. Berseneva, Yu.A. Gracheva, L.G. Dubova, P.N. Shevtsov, O.M. Redkozubova, E.F. Shevtsova, V.A. Tafeenko, L.A. Aslanov, E.R. Milaeva, Cytotoxic activity of organotin carboxylates based on synthetic phenolic antioxidants and polycyclic bile acids, J. Organomet. Chem. 909 (2020) 121089.
[13] J.K. Millet, G.R. Whittaker, Host cell proteases: critical determinants of coronavirus tropism and pathogenesis, Virus Res. 202 (2015) 120–134.
[14] B.J. Bosch, R. Zee, C.A.M. Haan, P.J.M. Rottier, The coronavirus spike protein is a class I virus fusion protein: structural and functional characterization of the fusion core complex, J. Virol. 77 (2003) 8801–8811.
[15] X.-Yi Ge, J.-L. Li, X.-.L. Yang, A.A. Chmura, G. Zhu, J.H. Epstein, J.K. Mazet, B. Hu, W. Zhang, C. Peng, Yu-Ji Zhang, C.-.M. Luo, B. Tan, N. Wang, Y. Zhu, G. Crameri, S-Yi Zhang, L-Fa Wang, P. Daszak, Z-Li Shi, Isolation and characterization of a bat SARS-like coronavirus that uses the ACE2 receptor, Nature 503 (2013) 535–538.
[16] X. Xu, P. Chen, J. Wang, J. Feng, H. Zhou, X. Li, Wu Zhong, P. Hao, Evolution of the novel coronavirus from the ongoing Wuhan outbreak and modeling of its spike protein for risk of human transmission, Sci. China Life Sci. 63 (2020) 457–460.
[17] J. Lan, J. Ge, J. Yu, S. Shan, H. Zhou, S. Fan, Q. Zhang, X. Shi, Q. Wang, L. Zhang, X. Wang, Structure of the SARS-CoV-2 spike receptor-binding domain bound to the ACE2 Receptor, Nature 581 (2020) 215–220.
[18] C.L. Armarego, Chai, in: Purification of Laboratory Chemicals, Butterworth-Heinemann, 2003, p. 415.
[19] G.M. Sheldrick, Acta Crystallogr. A 64 (2008) 112–122.
[20] Molecular Operating Environment MOEC.C.G.I.M, Quebec Canada, MOE-Dock, Chemical Computing Group. 2016. Inc., Montreal Quebec Canada, 2016.
[21] M.J. Frisch, G.W. Trucks, H.B. Schlegel, G.E. Scuseria, M.A. Robb, J.R. Cheeseman, J.A. Montgomery Jr., T. Vreven, K.N. Kudin, J.C. Burant, J.M. Millam, S.S. Iyengar, J. Tomasi, V. Barone, B. Mennucci, M. Cossi, G. Scalmani, N. Rega, G.A. Petersson, H. Nakatsuji, M. Hada, M. Ehara, K. Toyota, R. Fukuda, J. Hasegawa, M. Ishida, T. Nakajima, Y. Honda, O. Kitao, H. Nakai, M. Klene, X. Li, J.E. Knox, H.P. Hratchian, J.B. Cross, C. Adamo, J. Jaramillo, R. Gomperts, R.E. Stratmann, O. Yazyev, A.J. Austin, R. Cammi, C. Pomelli, J.W. Ochterski, P.Y. Ayala, K. Morokuma, G.A. Voth, P. Salvador, J.J. Dannenberg, V.G. Zakrzewski, S. Dapprich, A.D. Daniels, M.C. Strain, O. Farkas, D.K. Malick, A.D. Rabuck, K. Raghavachari, J.B. Foresman, J.V. Ortiz, Q. Cui, A.G. Baboul, S. Clifford, J. Cioslowski, B.B. Stefanov, G. Liu, A. Liashenko, P. Piskorz, I. Komaromi, R.L. Martin, D.J. Fox, T. Keith, M.A. Al-Laham, C.Y. Peng, A. Nanayakkara, M. Challacombe, P.M.W. Gill, B. Johnson, W. Chen, M.W. Wong, C. Gonzalez, J.A. Pople, Gaussian 09 (Linux version), 2009.
[22] R. Dennington, T. Keith, J. Millam, GaussView 5.0, Semichem Inc., 2009.
[23] F. Jensen, WIREs Comput. Mole. Sci. 3 (3) (2013) 273–295.
[24] T.H. Dunning Jr., P.J. Hay, in: Methods of Electronic Structure Theory, Springer, Boston, MA, 1977, pp. 1–27. Chapter 1.
[25] E.G. Lewars, Computational Chemistry: Introduction to the Theory and Applications of Molecular and Quantum Mechanics, 1st Edn., Springer, 2011.
[26] L. Touafri, A. Hellal, S. Chafaa, A. Khelifa, A. Kadri, Synthesis, characterisation and DFT studies of three Schiff bases derived from histamine, J. Mol. Struct. 1149 (2017) 750–760.
[27] C.W. Choi, S.C. Kim, S.S. Hwang, B.K. Choi, H.J. Ahn, M.Y. Lee, S.H. Park, S.K. Kim, Antioxidant activity and free radical scavenging capacity between Korean medicinal plants and flavonoids by assay-guided comparison, Plant Sci. 163 (2002) 1161–1168.
[28] R.L. Puntel, C.W. Nogueira, J.B.T. Rocha, Krebs cycle intermediates modulate thiobarbituric acid reactive species (TBARS) production in rat brain *in vitro*, Neurochem. Res. 30 (2005) 225–235.
[29] I.F.F. Benzie, J.J. Strain, Ferric reducing/antioxidant power assay: direct measure of total antioxidant activity of biological fuids and modifed version for simultaneous measurement of total antioxidant power and ascorbic acid concentration, Method Enzymol. 299 (1999) 15–27.
[30] EA. Uyoh, PN. Chukwurah, IA. David, AC. Bassey, Evaluation of antioxidant capacity of two Ocimum species consumed locally as spices in Nigeria as a justification for increased domestication, Am. J. Plant. Sci. 4 (2) (2013) 221–229.
[31] H. Chimi, J. Cillard, P. Cillard, M. Rahmani, Peroxyl and hydroxyl radical scavenging activity of some natural phenolic antioxidants, J. Am. Oil Chem. Soc. 68 (1991) 307–312.
[32] N. Muhammad, M. Ikram, F. Perveen, M. Ibrahim, M. Ibrahim, V. Abel, S. Rehman, S. Shujah, W. Khan, D.F. Shams, C. Schulzke, Syntheses, crystal structures and DNA binding potential of copper(II) carboxylates, J. Mol. Struct. 1196 (2019) 771–782.
[33] T.P. Lockhart, W.F. Manders, Inorg. Chem. 25 (1986) 892–895.
[34] AW. Addison, T.N Rao, J. Reedijk, J. van Rijn, GC. Verschoor, J. Chem. Soc. Dalton Trans. 7 (1984) 1349–1356.
[35] R. Guan, Z. Zhou, M. Zhang, H. Liu, W. Du, X. Tian, Q. Zhang, H. Zhou, J. Wu, Y. Tian, Organotin(IV) carboxylate complexes containing polyether oxygen chains with two-photon absorption in the near infrared region and their anticancer activity, Dyes Pigm. 158 (2018) 428–437.
[36] M. Sirajuddin, V. McKee, M. Tariq, S. Ali, Newly designed organotin(IV) carboxylates with peptide linkage: synthesis, structural elucidation, physicochemical characterizations and pharmacological investigations, Eur. J. Med. Chem. 143 (2018) 1903–1918.
[37] X. Xiao, X. Han, Z. Mei, D. Zhu, K. Shao, J. Liang, M. Tian, L. Xu, Organotin(IV) carboxylates based on amide carboxylic acids: syntheses, crystal structures and characterizations, J. Organomet. Chem. 729 (2013) 28–39.
[38] S.R. Wang, M. Arrowsmith, J. Böhnke, H. Braunschweig, T. Dellermann, R.D. Dewhurst, H. Kelch, I. Krummenacher, J.D. Mattock, J.H. Müssig, T. Thiess, A. Vargas, J. Zhang, Engineering a Small HOMO–LUMO Gap and Intramolecular C−H Borylation by Diborene/Anthracene Orbital Intercalation, Angew. Chem. Int. Ed. 56 (2017) 8009–8013.
[39] C.J. Cramer, D.G. Truhlar, Density functional theory for transition metals and transition metal chemistry, PCCP 11 (2009) 10757–10816.
[40] IT. Lima, L. Sousa, RS. Freitas, L.A. Ribeiro Junior, R.T. de Sousa Júnior, DA.S Filho, A DFT study of a set of natural dyes for organic electronics, J. Mol. Model. 23 (2017) 1–9.
[41] A.F. Butt, M.N. Ahmed, M.H. Bhatti, M.A. Choudhary, K. Ayub, M.N. Tahir, T. Mahmood, DFT studies, antimicrobial activities and DNA binding interactions of two newly synthesized organotin(IV) carboxylates, J. Mol. Struct. 1191 (2019) 291–300.
[42] F. Javed, M. Sirajuddin, S. Ali, N. Khalid, M.N. Tahir, N.A. Shah, Z. Rasheed, M.R. Khan, Organotin(IV) derivatives of o-isobutyl carbonodithioate: synthesis, spectroscopic characterization, X-ray structure, HOMO/LUMO and *in vitro* biological activities, Polyhedron 104 (2016) 80–90.
[43] A. Tarahhomi, A.V.D. Lee, A new six-coordinate organotin(IV) complex of $OP[NC_5H_{10}]_3$: a comparison with an analogous five-coordinate complex by means of X-ray crystallography, Hirshfeld surface analysis and DFT calculations, J. Coord. Chem. 71 (2018) 1575–1592.
[44] R.G. Pearson, Proc. Natl. Acad. Sci. 83 (1986) 8440–8441.
[45] R. Joshi, S. Kumar Yadav, N. Pandey, H. Mishra, R. Tilak, S. Pokharia, Combined experimental and theoretical studies on the diorganotin(IV) complexes of sparfloxacin: synthesis, spectroscopic and DFT studies, and biological activity, J. Mol. Struct. 1167 (2018) 44–56.
[46] R. Joshi, N. Pandey, R. Tilak, S. Kumar Yadav, H. Mishra, S. Pokharia, New triorganotin(IV) complexes of quinolone antibacterial drug sparfloxacin: synthesis, structural characterization, DFT studies and biological activity, Appl. Organomet. Chem. 32 (5) (2018) e4324.

[47] M.N. Ahmed, K.A. Yasin, K. Ayub, T. Mahmood, M. NawazTahir, B.A. Khan, M. Hafeez, M. Ahmed, Ihsanul-Haq. Click one pot synthesis, spectral analyses, crystal structures, DFT studies and brine shrimp cytotoxicity assay of two newly synthesized 1,4,5-trisubstituted 1,2,3-triazoles, J. Mol. Struct. 1106 (2016) 430–439.
[48] CA. Devaux, J.-.M. Rolain, P. Colson, D. Raoult, New insights on the antiviral effects of chloroquine against coronavirus: what to expect for COVID-19? Int. J. Antimicrob. Agents 55 (2020) 105938.
[49] P. Sun, X. Lu, C. Xu, W. Sun, B. Pan, Understanding of COVID-19 based on current evidence, J. Med. Virol. 92 (2020) 548–551.
[50] J.O. Adeyemi, D.C. Onwudiwe, A.C. Ekennia, C.P. Anokwuru, N. Nundkumar, M. Singh, E.C. Hosten, Synthesis, characterization and biological activities of organotin(IV) diallyldithiocarbamate complexes, Inorganica. Chim. Acta 485 (2019) 64–72.
[51] A. Corona-Bustamante, J.M. Viveros-Paredes, A. Flores-Parra, A.L. Peraza-Campos, F.J. Martínez-Martínez, M.T. Sumaya-Martínez, Á. Ramos-Organillo, Antioxidant activity of butyl- and phenylstannoxanes derived from 2-, 3- and 4-pyridinecarboxylic acids, Molecules 15 (2010) 5445–5459.